WILEY-VCH

DOI: 10.1002/((please add manuscript number))
**Article type: Communication**

# Anisotropic $MoS_2$ nanosheets grown on self-organized nanopatterned substrates

*Christian Martella*, Carlo Mennucci, Eugenio Cinquanta, Alessio Lamperti, Emmanuele Cappelluti, Francesco Buatier de Mongeot and Alessandro Molle**

Dr. C. Martella, Dr. E. Cinquanta§, Dr. A. Lamperti, Dr. A. Molle
Laboratorio MDM, IMM-CNR, via C. Olivetti 2, I-20864, Agrate Brianza (MB), Italy
E-mail: christian.martella@mdm.imm.cnr.it, alessandro.molle@mdm.imm.cnr.it
§ Present Address: Dipartimento di Fisica, Politecnico di Milano, Piazza L. da Vinci 32, 20133 Milano, Italy
Dr. C. Mennucci, Prof. F. Buatier de Mongeot
Dipartimento di Fisica, Università di Genova, via Dodecaneso 33, I-16146, Genova (Ge), Italy
Dr. E. Cappelluti
Istituto dei Sistemi Complessi (ISC)-CNR, U.O.S. Sapienza, 00185 Roma, Italy and
Dipartimento di Fisica, Università "La Sapienza", P.le A. Moro 2, I-00185 Roma, Italy

Keywords: two-dimensional materials, anisotropy, molybdenum disulfide, transition metal dichalcogenides, self-organised nanopatterning

Manipulating the anisotropy in two-dimensional nanosheets is a promising way to tune or trigger functional properties at the nanoscale. Here, a novel approach is presented to introduce a one-directional anisotropy in $MoS_2$ nanosheets via chemical vapor deposition (CVD) onto rippled patterns prepared on ion-sputtered $SiO_2$/Si substrates. The opto-electronic properties of $MoS_2$ are dramatically affected by the rippled $MoS_2$ morphology both at the macro- and the nano-scale. In particular, strongly anisotropic phonon modes are observed depending on the polarization orientation with respect to the ripple axis. Moreover, the rippled morphology induces localization of strain and charge doping at the nanoscale, thus causing substantial red shifts of the phonon mode frequencies and a topography-dependent modulation of the $MoS_2$ workfunction, respectively. Our study paves the way to a controllable tuning of the anisotropy via substrate pattern engineering in CVD-grown two-dimensional nanosheets.

Main Text

Introducing anisotropic structural modifications may offer a tool to engineer novel functional properties in two-dimensional (2D) crystal nanosheets. For instance, in graphene and Transition Metal Dichalcogenides (TMDs), nanoscale anisotropy was shown to induce modifications of the physical properties including band-gap opening, distortion of the electronic band structure, dichroic light absorption, magnetic moment transitions, exciton potential confinement and semiconductor-to-metal phase transitions.[1–9] Manipulating the anisotropy in TMD nanosheets can expand or boost the opto-electronic performances as reported in field-effect transistors and photodetectors.[10,11] So far, anisotropy in TMDs nanosheets has been artificially induced by processing exfoliated flakes into nanoscale patterns (ribbons, meshes, ripples, etc.) by means of lithographic approaches, or by applying uni-axial strain deformations exploiting a stressed elastomeric substrate.[5,8,12–15] Here, we expose a novel approach to introduce strongly anisotropic rippled modulations and atomically thin 2D nanosheets, taking the molybdenum disulfide ($MoS_2$) as a case study. Since the chemical vapour deposition (CVD) of $MoS_2$ nanosheets provides a high degree of conformality to the substrate and thickness control at the atomic level, we implemented the CVD growth of the $MoS_2$ nanosheets on a large area ($cm^2$-scale) pre-patterned rippled silicon dioxide ($SiO_2$) on silicon substrate obtained by grazing angle defocused ion beam sputtering (see **Experimental Section** and **Supplementary Information**).[16–22] The formation of the $MoS_2$ nanosheets is inferred from the X-ray photoelectron spectroscopy (XPS) study of the Mo and S photoemission core levels. The XPS spectra of **Figure 1 a** show that the $MoS_2$ nanosheets possess the same trigonal prismatic coordination typical of the 2H semiconductor phase and the same chemical constitution irrespective of the rippled or flat substrate.[23] The AFM investigations depicted in **Figure 1 b** compare the isotropic morphology of the $MoS_2$

nanosheets grown on flat $SiO_2$/Si substrate (inset) with the anisotropic uni-axial morphology achieved when the same nanosheets are grown on the rippled pattern. The linear cuts allow us to appreciate the height variations in the rippled nanosheets, with a crest-to-valley amplitude in the range of 200-300 nm, compared to the smooth profile of the flat sample. Remarkably, the cross-sectional Transmission Electron Microscopy (TEM) images of **Figure 1 c** show that a layered $MoS_2$ can be grown conformally on both substrates. Moreover, the $MoS_2$ layers adapt to the local curvature of the surface modulations in the case of the rippled substrate. In both samples, a number of four $MoS_2$ layers is inferred from the zoomed-in view of the TEM images shown in the insets of **Figure 1 c**. We used Raman spectroscopy to investigate the anisotropic character of the rippled sample on the macroscale.[5,24] The spectra plotted in **Figure 2 a** and **b,c** show the distinctive in-plane, $E^1_{2g}$, and out-of-plane, $A_{1g}$, vibrational modes of the flat and rippled $MoS_2$, respectively.[24] In both cases, the Raman modes, located at frequency $\omega(E^1_{2g}) \sim 383$ cm$^{-1}$ and $\omega(A_{1g}) \sim 407$ cm$^{-1}$, exhibits a frequency separation ($\Delta\omega \sim 24$ cm$^{-1}$) consistent with four layers thick $MoS_2$ nanosheets in agreement with the information inferred from the TEM images.[24] The Raman spectra of the flat nanosheets, **Figure 2 a**, present an invariant response for orthogonal orientations of the sample respect to the polarization direction of the laser beam (black straight line and star symbols). On the contrary, the rippled nanosheets show a striking anisotropic behavior when $\vartheta$, the angle between the polarization direction and the ripple main axis, is varied from 0° to 90° by changing the in-plane orientation of the sample mounted on a rotating stage (**Figure 2 b** and **c**, respectively). It is worth noting that the contribution of the dichroic optical reflectivity of the rippled pattern to the observed Raman anisotropy is negligible as far as the anisotropic variation measured in the reflectance spectra is at least one order of magnitude smaller than the one observed in the Raman peak intensity (see **Supporting Information**). [25] In detail, the intensity of the Raman modes is strongly amplified for light polarized along the direction of the ripple periodicity, namely for $\vartheta$=90°. This fact is clearly evidenced by the polar

diagram of the $E^1_{2g}$ and $A_{1g}$ peak intensity plotted as a function of the $\vartheta$ angle. Both signals (gray squares) in **Figure 2 d** and **e** appear with two-lobe behavior orthogonal to the ripple ridge direction ($\vartheta$=90° and 270°) and with an angular distribution qualitatively described by a $\sim \sin^2(\vartheta)$ trigonometric law (red curves). The polarization dependence also influences the peak intensity ratio, $I(A_{1g})/I(E^1_{2g})$, which reads ~1 and ~ 2 for the parallel and orthogonal orientations, respectively. The above experimental results can be rationalized in terms of the uniaxial deformation of the long range order of the atomic planes due to the anisotropic rippled morphology, which affects inter- and intra-plane phonon coupling, in agreement with previous reports on the optical phonon properties of $MoS_2$ nanoribbons.[5] The optical anisotropy inferred from the polarized Raman measurements is also reflected at the local scale when probing the sample by means of micro-Raman spectroscopy operating in confocal mode and laser polarization orthogonal to the ripple main axis (see **Experimental Section** for details about the measurements). **Figure 3 a** and **b** illustrate the Raman maps of the frequency shifts of the $E^1_{2g}$ and $A_{1g}$ modes with respect to their spectral positions in the flat sample. Note that the Raman maps are superimposed on the optical picture of the surface thus allowing for a straightforward match with the nanosheet morphology. Remarkably, both maps show strongly anisotropic domains which reproduce the morphological features of the rippled surface. Large frequency shifts are observed in the direction of the pattern periodicity, in particular among the crests and the valleys of the ripples. Interestingly, red shifts (i.e. negative shifts) of both the $E^1_{2g}$ and $A_{1g}$ phonon modes are observed in correspondence of the valleys of the ripples, while the mode positions at the crest are nearly comparable with those of the reference sample. Apparently, the $E^1_{2g}$ and $A_{1g}$ modes are red-shifted by a similar amount. This fact indicates a constant frequency separation between the two modes, and hence no change of the thickness in the $MoS_2$ nanosheet.[24] The physical origin of the $E^1_{2g}$ mode frequency shift in $MoS_2$ is commonly associated to strain localized into the layers of the nanosheets.[14,15] If so, the measured red-shift for the $E^1_{2g}$ mode (~ -4.5 $cm^{-1}$) is consistent

with the incorporation of a tensile strain field into the nanosheets of the order of ~ 2.5-3%, opposite to the compressive strain observed in the ripple valleys obtained deforming $MoS_2$ nanosheets exfoliated onto elastic substrates. [8,15,26] On the other hand, the observed red-shift of the $A_{1g}$ mode (~ -3.7 $cm^{-1}$) reveals that an intrinsic anisotropic charge (electron/hole) modulation occurs in the $MoS_2$ nanosheets as a function of the surface profile. [27] We verified the local charge modulation by probing the contact potential distribution (CPD) between a conductive Pt/Ir AFM-tip and the $MoS_2$ nanosheets electrically grounding the sample surface for Kelvin-Probe AFM measurements (KPFM) (see the sketch in **Figure 4 a**). Since the CPD signal is a measure of the relative difference between the surface Fermi level of the sample and of the tip, the emergence of local charge doping can be directly inspected via CPD mapping. [28] **Figure 4 b** and **c** respectively show the (simultaneously acquired) topography and the potential maps of the rippled $MoS_2$. The CPD map clearly shows how the potential undergoes spatial modulations in the same direction of the ripples of the $MoS_2$ nanosheets. The induced anisotropy of the local potential can be quantitatively characterized by evaluating the self-correlation function of the CPD, $\chi_{CPD}$, along the x- and y-axis shown in the inset of **Figure 4 c**. The decay of the self-correlation function gives a rough estimate of the size of the one-directional patterns in the CPD map in the respective directions, whereas the oscillating behavior reveals the underlying periodicity (see the inset of **Figure 4 e**). Conversely, a clear-cut isotropic distribution comes up from the self-correlation function of the CPD probed on the flat nanosheets (See **Supporting Information**). The correlation between the local potential and the underlying topology of the $MoS_2$ nanosheets is furthermore pointed out by analyzing the cross-correlation function between the CPD and the topographic maps, $\chi_{h,CPD}$, as reported in **Figure 4 d**. Although the highest cross-correlation, at the local scale x=y=0, is quite moderate ( $\chi_{h,CPD}(0,0) \approx -0.22$ ), the anisotropy emerges from the different behavior along the x- and y-directions inferred from the linear cuts shown in **Figure 4 e**. In particular,

the long decay of the cross-correlation function along y, on a scale of ~0.5 μm, shows that a controlled patterning of the electrostatic properties of $MoS_2$ nanosheets on a micro-scale is in principle feasible. The negative value at the local scale suggests that morphological valleys have statistically larger CPDs. This finding is further corroborated by a comparative analysis of the CPD and topographic maps. Indeed, if we select only those regions where CPD is larger than a threshold value, we find out that the average height in the corresponding topographic map reduces as the threshold value increases. At the same time, the negative local cross-correlation increases up to ~-0.4 (for CPD threshold $\geq$ 0.9 V). In agreement with the Raman mapping in **Figure 3**, the CPD maps shows a local charge modulation which stems from the anisotropic spatial modulation of the nanosheets. In particular, the large CPD values at the valleys correspond to a reduction of the $MoS_2$ workfunction and hence to an electron doping (the CPD signal can be recast as a local measure of the material workfunction by calibrating the AFM tip, see **Experimental Section**). An indirect confirmation of this picture is given by the analysis of the work-function distribution histogram, as shown in **Figure 4 f** for the flat $MoS_2$ and in **Figure 4 g** for the rippled nanosheets. In case of the flat nanosheets, the work-function distribution exhibits a symmetric Gaussian profile peaked at~ 5.06 eV, in agreement with previously reported results.[29] On the other hand, the work-function distribution for the rippled $MoS_2$ nanosheets differs from the flat case in the central peak position, which is shifted by ~ -0.2 eV, and in the appearance of two more Gaussian sub-distributions, centered at ~ 5.5 eV and 4.6 eV. In the light of the finite correlation with the topography, it is interesting to relate these two Gaussian distributions to topographic regions with local hole and electron doping, respectively. This behavior can be associated with the formation of electrically active defects during $MoS_2$ growth onto the rippled pattern. [30]

In conclusion, we have shown that strongly anisotropic $MoS_2$ nanosheets can be grown on one-directional ripple pattern substrates via CVD deposition. At the macroscopic scale, the so-induced morphological anisotropy results in a sharp polarization-dependent excitation of the Raman active phonon modes with respect to ripple axis. On the local scale, we showed a morphology-dependent variability of the optical and electronic properties of the $MoS_2$, which leads to phonon mode shifts and local charge doping. Even though the physical origin of the observed opto-electronic anisotropy is not fully understood and further investigations are needed to elucidate specific effects related to the nanoscale rippled morphology (e.g. strain localization, electronic band distortion, etc.), our present findings pave the way to on-demand design of anisotropic 2D layered materials or heterostructures, being the CVD grown easily extendible to other TMDs. The degree of freedom offered by the pattern design in the artificial tailoring of the photonic, electronic and mechanical properties of TMDs may expand their range of applicability, in particular where an anisotropic character is desirable, like, for instance, thermoelectric devices, atomically thin optical polarizers, piezoelectric sensors. [31–33]

**Experimental Section**

*Sample fabrication*. A 150 nm thick polycrystalline Au film was deposited on a $SiO_2$ substrate by thermal evaporation from an alumina crucible at a constant flux of 6 nm/min calibrated by means of a quartz microbalance. The as-deposited film was exposed to defocused ion beam irradiation from a gridded multiaperture $Ar^+$ source (Tectra instruments) at a constant flux $\sim 4.95 \times 10^{15}$ ions/cm$^2$ s (measured in a plane orthogonal to the beam direction) and an energy of 800 eV. A biased tungsten filament ($V_{bias} = -13$ V), providing electrons via thermoionic emission, was placed close to the extraction grid in order to compensate surface charging effects due to ion irradiation. Adopting a grazing incidence irradiation geometry (82° with respect to the substrate normal), a self-organized ripple pattern, with a main axis oriented

along the ion beam projection direction, developed at the surface of the metal film due to the competition of ion-erosion and atom surface diffusion. Ion irradiation was prolonged until the complete removal of the self-organized gold mask thus projecting the nanopattern into the $SiO_2$ substrate.

For the $MoS_2$ growth, a 4 nm thick molybdenum oxide film was e-beam evaporated on the nanopatterned and flat $SiO_2$ substrates. The as-deposited films were used as molybdenum precursors in a sulfurization process carried out in a hot wall tubular furnace in a chemical vapor deposition approach. The precursors were inserted at the centre of a quartz tube and heated up to 850°C while sulphur vapours were induced by the evaporation of sulphur powder and carried towards the molybdenum precursor by an argon flux (0.2-0.3 L/h).

*Characterization.* XPS measurements were performed on a PHI 5600 instrument equipped with a monochromatic Al Kα x-ray source (energy = 1486.6 eV) and a concentric hemispherical analyser. The spectra were collected at a take-off angle of 45° and band-pass energy of 23.50 eV. The instrument resolution was 0.5 eV. The spectra were aligned using C1s (285 eV) as reference.

Polarized Raman spectroscopy measurements were performed in a backscattering configuration employing a Renishaw InVia spectrometer, equipped with the 514 nm (2.41 eV) line of an $Ar^+$ laser. The laser radiation was focused on the sample by means of a 50x Leica objective (0.75 numerical aperture), maintaining the incident laser power below 1 mW to avoid sample damage. Raman mapping measurements were conducted using Renishaw InVia Raman confocal microscope in the Renishaw StreamHR$^{TM}$ technique. The spectrometer was operated in high confocal mode with a 532 nm laser radiation coupled to a 150x objective. The spectroscopic maps were acquired over a 10 μm x 8 μm sample area with the polarization direction orthogonal to the main axis of the ripples. The sampling interval was 100 nm and the spatial resolution achievable by the confocal configuration can be assessed in ~336 nm.

The morphology of the samples was investigated in tapping mode by means of an AFM-Bruker commercial system, equipped with ultra-sharp silicon probes (nominal tip radius < 10 nm). All the AFM maps were acquired with the fast scanning direction of the microscope aligned orthogonally to the main axis of the nanostructures, thus allowing calculation of the statistical functions of the patterns over the image rows. The KPFM measurements were carried out in a dual frequency configuration allowing the simultaneous acquisition of topographic and CPD signal. The Pt/Ir coated tip was kept in mechanical oscillation at frequency $f_0$~70 kHz, while an oscillating voltage (amplitude = 3 V) at frequency $f_1$~ 6 kHz was applied to the tip. The sample surface was electrically grounded by means of the microscope sample holder. It was also possible to transform the CPD signal in a measure of the workfunction (Φ) distribution in the $MoS_2$ nanosheets according to the equation:

$$\Phi_{sample} = \Phi_{tip} - e \cdot CPD$$

Where $\Phi_{tip}$ is the tip work function derived by calibrating the AFM tip on a reference gold sample (assuming a 5.1 eV workfunction for gold).

**Supporting Information**
Supporting Information is available from the Wiley Online Library or from the author.

**Acknowledgements**
Carlo Grazianetti, Massimo Longo and Fabio Pezzoli are acknowledged for fruitful scientific discussions. Mario Alia, Alessio Cirone and Riccardo Tagliapietra are acknowledged for technical support. Dr. Tim Batten is acknowledged for the confocal Raman mapping measurements carried out at the Spectroscopy Product Division, Renishaw Plc, Wotton-under-Edge, Gloucestershire (UK). Davide Codegoni and Paolo Targa at STMicroelectronics-Agrate Brianza are acknowledged for TEM measurements. C.Mennucci and F.Buatier de Mongeot would like to thank the financial support of Compagnia di San Paolo in the framework of Project ID ROL 9361 and of MAECI in the framework of the Italy-Egypt bilateral protocol. E.Cappelluti acknowledges support from the European project FP7-PEOPLE-2013-CIG "LSIE 2D", and from the Italian MIUR program "Progetto Premiale

2012", Project ABNANOTECH. This research is partially funded by the MIUR under the PRIN 2015 grant 2015WTW7J3. All authors have given approval to the final version of the manuscript.

Received: ((will be filled in by the editorial staff))
Revised: ((will be filled in by the editorial staff))
Published online: ((will be filled in by the editorial staff))

References

[1] M. Y. Han, B. Özyilmaz, Y. Zhang, P. Kim, *Phys. Rev. Lett.* **2007**, *98*, 206805.

[2] Z. H. Ni, T. Yu, Y. H. Lu, Y. Y. Wang, Y. P. Feng, Z. X. Shen, *ACS Nano* **2008**, *2*, 2301.

[3] J. Bai, X. Zhong, S. Jiang, Y. Huang, X. Duan, *Nat. Nanotechnol.* **2010**, *5*, 190.

[4] H. Pan, Y.-W. Zhang, *J. Mater. Chem.* **2012**, *22*, 7280.

[5] J.-B. Wu, H. Zhao, Y. Li, D. Ohlberg, W. Shi, W. Wu, H. Wang, P.-H. Tan, *Adv. Opt. Mater.* **2016**, *4*, 756.

[6] J. Quereda, P. San-Jose, V. Parente, L. Vaquero-Garzon, A. J. Molina-Mendoza, N. Agraït, G. Rubio-Bollinger, F. Guinea, R. Roldán, A. Castellanos-Gomez, *Nano Lett.* **2016**, *16*, 2931.

[7] L. Kou, C. Tang, Y. Zhang, T. Heine, C. Chen, T. Frauenheim, *J. Phys. Chem. Lett.* **2012**, *3*, 2934.

[8] A. Castellanos-Gomez, R. Roldán, E. Cappelluti, M. Buscema, F. Guinea, H. S. J. van der Zant, G. A. Steele, *Nano Lett.* **2013**, *13*, 5361.

[9] E. Scalise, M. Houssa, G. Pourtois, V. Afanas'ev, A. Stesmans, *Nano Res.* **2012**, *5*, 43.

[10] B. Radisavljevic, A. Radenovic, J. Brivio, V. Giacometti, A. Kis, *Nat. Nanotechnol.* **2011**, *6*, 147.

[11] G. Fiori, F. Bonaccorso, G. Iannaccone, T. Palacios, D. Neumaier, A. Seabaugh, S. K. Banerjee, L. Colombo, *Nat. Nanotechnol.* **2014**, *9*, 768.

[12] D. S. Fox, Y. Zhou, P. Maguire, A. O'Neill, C. Ó'Coileáin, R. Gatensby, A. M.

Glushenkov, T. Tao, G. S. Duesberg, I. V. Shvets, M. Abid, M. Abid, H.-C. Wu, Y. Chen, J. N. Coleman, J. F. Donegan, H. Zhang, *Nano Lett.* **2015**, *15*, 5307.

[13] H. Nam, S. Wi, H. Rokni, M. Chen, G. Priessnitz, W. Lu, X. Liang, *ACS Nano* **2013**, *7*, 5870.

[14] Y. Wang, C. Cong, C. Qiu, T. Yu, *Small* **2013**, *9*, 2857.

[15] C. Rice, R. J. Young, R. Zan, U. Bangert, D. Wolverson, T. Georgiou, R. Jalil, K. S. Novoselov, *Phys. Rev. B* **2013**, *87*, 081307.

[16] Y. Zhan, Z. Liu, S. Najmaei, P. M. Ajayan, J. Lou, *Small* **2012**, *8*, 966.

[17] K.-K. Liu, W. Zhang, Y.-H. Lee, Y.-C. Lin, M.-T. Chang, C.-Y. Su, C.-S. Chang, H. Li, Y. Shi, H. Zhang, C.-S. Lai, L.-J. Li, *Nano Lett.* **2012**, *12*, 1538.

[18] X. Ling, Y.-H. Lee, Y. Lin, W. Fang, L. Yu, M. S. Dresselhaus, J. Kong, *Nano Lett.* **2014**, *14*, 464.

[19] S. Najmaei, Z. Liu, W. Zhou, X. Zou, G. Shi, S. Lei, B. I. Yakobson, J.-C. Idrobo, P. M. Ajayan, J. Lou, *Nat. Mater.* **2013**, *12*, 754.

[20] D. Chiappe, A. Toma, Z. Zhang, C. Boragno, F. Buatier de Mongeot, *Appl. Phys. Lett.* **2010**, *97*, 053102.

[21] A. Toma, B. S. Batič, D. Chiappe, C. Boragno, U. Valbusa, M. Godec, M. Jenko, F. Buatier de Mongeot, *J. Appl. Phys.* **2008**, *104*, 104313.

[22] S. Vangelista, E. Cinquanta, C. Martella, M. Alia, M. Longo, A. Lamperti, R. Mantovan, F. B. Basset, F. Pezzoli, A. Molle, *Nanotechnology* **2016**, *27*, 175703.

[23] H. Liu, K. K. Ansah Antwi, J. Ying, S. Chua, D. Chi, *Nanotechnology* **2014**, *25*, 405702.

[24] C. Lee, H. Yan, L. E. Brus, T. F. Heinz, J. Hone, S. Ryu, *ACS Nano* **2010**, *4*, 2695.

[25] C. Martella, D. Chiappe, C. Mennucci, F. B. de Mongeot, *J. Appl. Phys.* **2014**, *115*, 194308.

[26] A. Michail, N. Delikoukos, J. Parthenios, C. Galiotis, K. Papagelis, *Appl. Phys. Lett.*

**2016**, *108*, 173102.

[27] B. Chakraborty, A. Bera, D. V. S. Muthu, S. Bhowmick, U. V. Waghmare, A. K. Sood, *Phys. Rev. B* **2012**, *85*, 161403.

[28] M. Nonnenmacher, M. P. O'Boyle, H. K. Wickramasinghe, *Appl. Phys. Lett.* **1991**, *58*, 2921.

[29] J. H. Kim, J. Lee, J. H. Kim, C. C. Hwang, C. Lee, J. Y. Park, *Appl. Phys. Lett.* **2015**, *106*, 251606.

[30] Z. Lin, B. R. Carvalho, E. Kahn, R. Lv, R. Rao, H. Terrones, M. A. Pimenta, M. Terrones, *2D Mater.* **2016**, *3*, 022002.

[31] A. Arab, Q. Li, *Sci. Rep.* **2015**, *5*, 13706.

[32] F. Xia, H. Wang, Y. Jia, *Nat. Commun.* **2014**, *5*, 666.

[33] J. Qi, Y.-W. Lan, A. Z. Stieg, J.-H. Chen, Y.-L. Zhong, L.-J. Li, C.-D. Chen, Y. Zhang, K. L. Wang, *Nat. Commun.* **2015**, *6*, 7430.

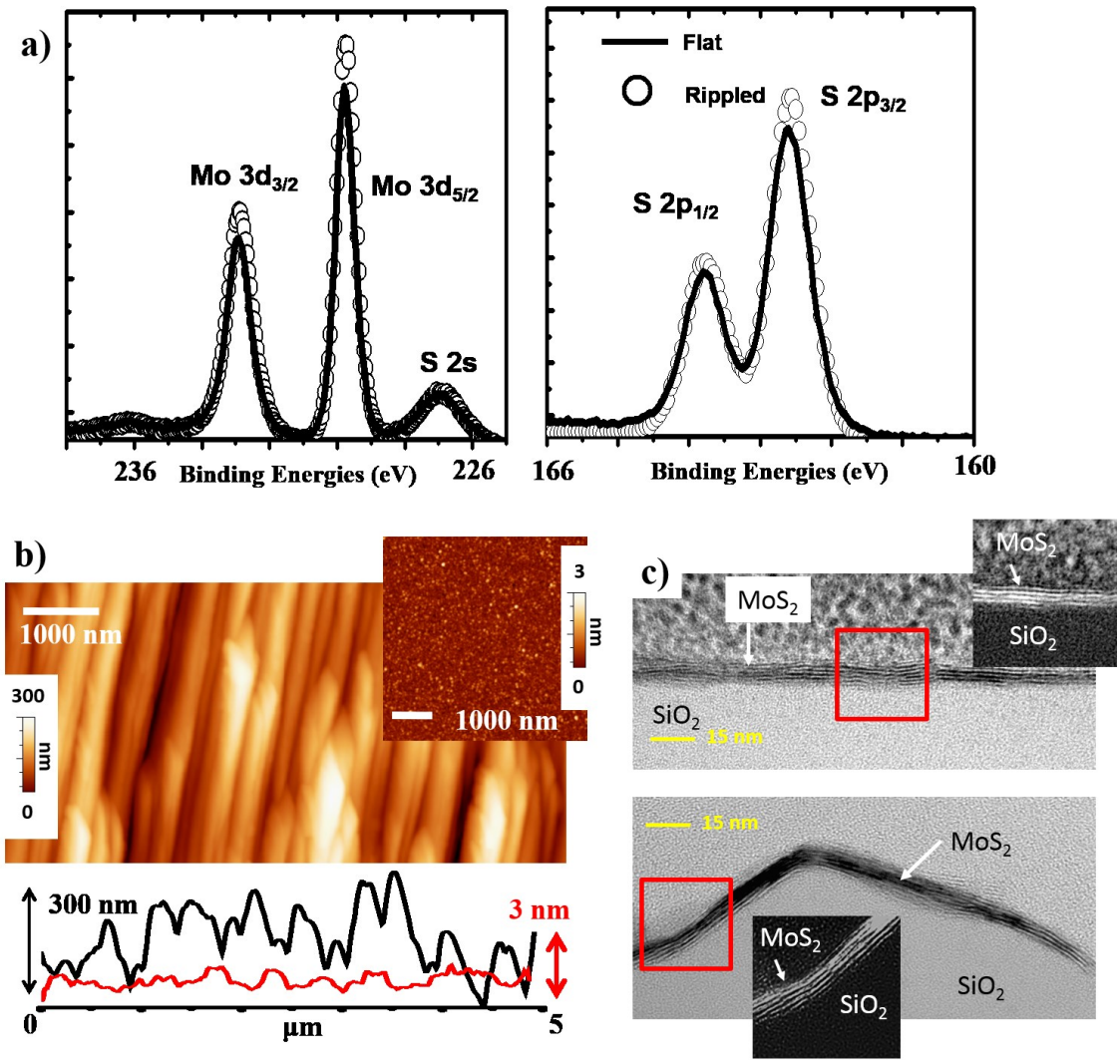


**Figure 1.** (a) XPS analysis of the Mo *3d*, S *2s* and S *2p* core levels of the $MoS_2$ nanosheets grown on flat (open circles) and rippled (straight line) substrates (b) AFM topography of the rippled and flat (inset) $MoS_2$ nanosheets. At the bottom: representative height profiles extracted from the topographic maps (c) Cross sectional TEM images of the flat (top) and rippled (bottom) nanosheets. The insets show a zoomed-in view of the red squares in figures. Note that the $MoS_2$ layers are clearly visible (in the insets colors are inverted to enhance the contrast.)

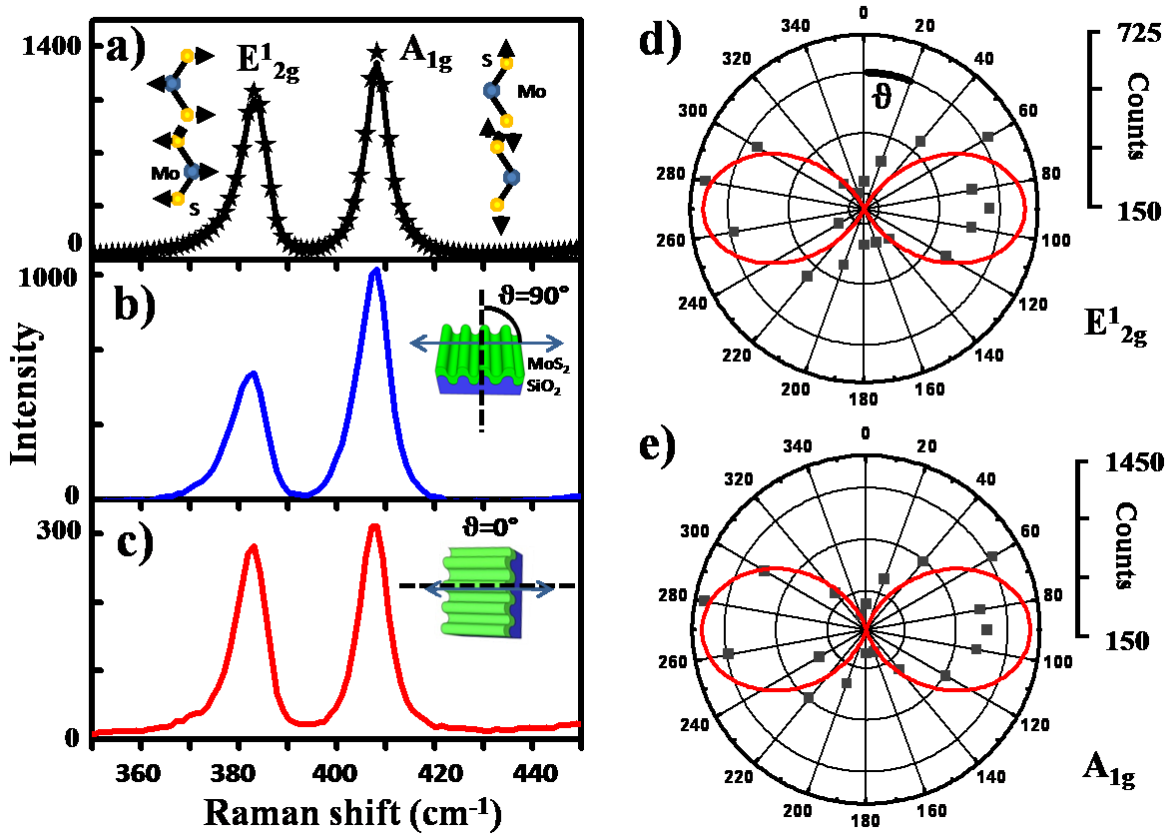


**Figure 2.** (a) Polarized Raman spectra of the reference $MoS_2$ nanosheets grown on flat $SiO_2$. Black straight line and stars symbols correspond to orthogonal orientations of the sample. (b) and (c) Polarized Raman spectra of the rippled $MoS_2$ nanosheets for orientation of the ripples axis orthogonal and parallel to the laser polarization respectively, see insets. Polar plots of the peak intensity of the (d) $E^1_{2g}$ and (e) $A_{1g}$ Raman modes as a function of the angle, ϑ, between the laser polarization and the ripples axis. The red traces are proportional to the $\sim\sin^2(\vartheta)$ trigonometric function.

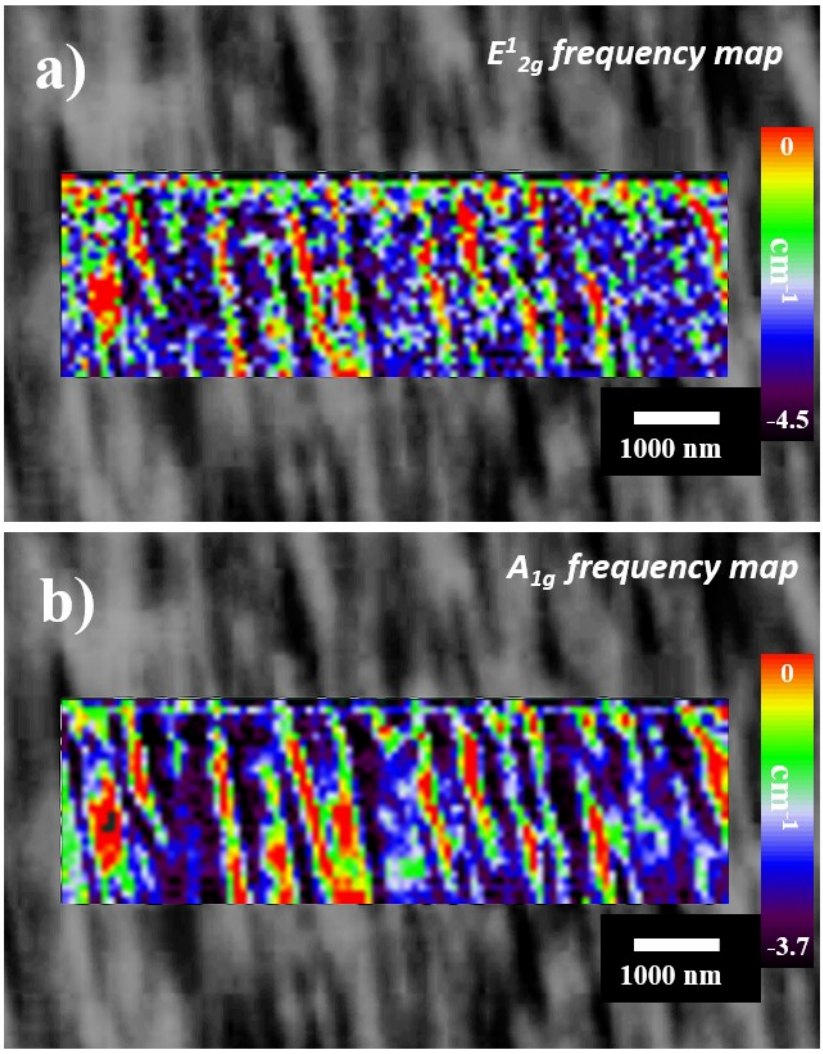


**Figure 3.** (a) and (b) High resolution confocal Raman maps of the frequency positions of the $E^1_{2g}$ and $A_{1g}$ modes, respectively. Both maps are acquired with laser polarization orthogonal to the ripple main axis. Notice that the Raman maps are superimposed on the corresponding optical images of the surface so as to emphasize the correlation between the rippled morphology and the Raman map.

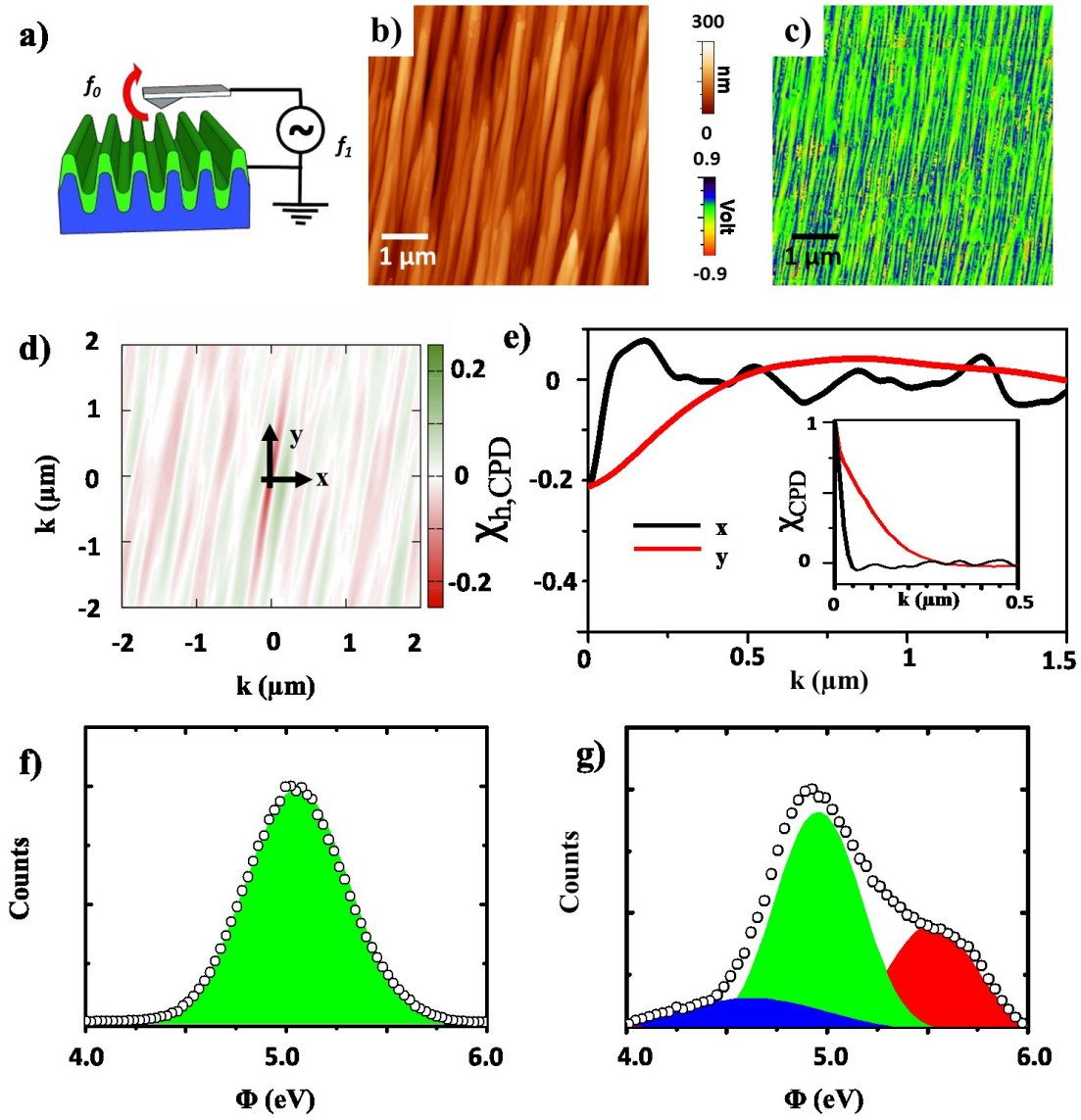


**Figure 4.** (a) Sketch of the Kelvin-probe force microscopy experimental setup for the acquisition of the contact potential distribution (CPD). The surface of the sample is electrically grounded, while an AC voltage oscillating at frequency $f_1$ is applied to the Pt/Ir tip of an atomic force microscope. The tip is also kept in mechanical oscillation at frequency $f_0$ for the simultaneous acquisition of the sample topography. (b) Topography of the rippled $MoS_2$ nanosheets acquired simultaneously to the (c) CPD map. (d) cross-correlation function between the topographic and CPD maps shown in (b) and (c) respectively. (e) linear cuts of the cross-correlation function along the x- and y-axis shown in (d). Inset: self-correlation function of the CPD map. f) and g) workfunction distributions calculated from the CPD signal acquired on the flat and rippled $MoS_2$ nanosheets respectively.

Keyword

C. Martella*, C. Mennucci, E. Cinquanta, A. Lamperti, E. Cappelluti, F. Buatier de Mongeot and A. Molle*

**Anisotropic $MoS_2$ nanosheets grown on self-organized nanopatterned substrates**

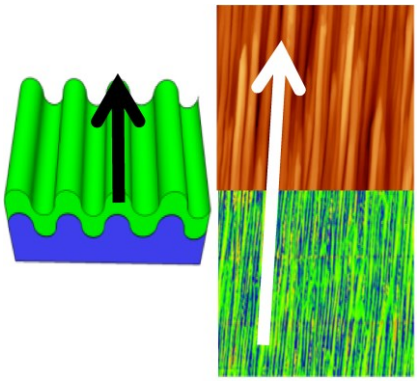

# Supporting Information

## Anisotropic $MoS_2$ nanosheets grown on self-organized nanopatterned substrates

*Christian Martella*, Carlo Mennucci, Eugenio Cinquanta, Alessio Lamperti, Emmanuele Cappelluti, Francesco Buatier de Mongeot and Alessandro Molle**

**Substrate patterning.** Defocused Ion Beam Sputtering (IBS) has been employed to form a nanoscale pattern of one-directional ripples on the silica substrate. The process takes advantage from self-organized mechanisms induced adopting a grazing incidence $Ar^+$ sputtering condition (82° off-normal) and exploiting a sacrificial metallic mask.[1,2] In detail, the mask is formed starting from a 150nm-thick Au film thermally evaporated on the $SiO_2$ substrate before IBS. The interplay between diffusive and erosive mechanisms leads to the formation of a ripple pattern at the surface of the Au film (sketch in **Figure S1 a**). Due to the preferential sputter erosion of the valleys of the ripples respect to the crests, the rippled pattern rapidly evolves into an array of Au nanowires (NWs) laterally disconnected, which represents the sacrificial stencil mask (sketch in **Figure S1 b**). Once the NWs are created, the harsh ion etching of the substrate, in correspondence of the gap between nanowires, induces the formation of deep valleys into the substrate. This is the case of substrate materials, such as $SiO_2$, which are characterized by a higher sputtering yield respect to gold, and thus they are eroded much faster than the metal.[1] The AFM measurements, shown in **Figure S1 c** and **d**, depict the mask formation. To better show the gold and $SiO_2$ regions, a mechanical scratch has been made into the metal by means of a micrometric tip. The yellow colored structures in **Figure S1 d** represent the Au nanowires lying above the level of the substrate, identified from the red dashed line. It is easy to note that deep trenches are etched into the $SiO_2$ by the sputtering process. The NWs extend for microns in the direction of the ion flux projection (vertical axis of **Figure S1 c**), their lateral size is broad distributed in the range 150 nm- 500 nm, as a consequence of the intrinsic randomness of the ion impacts.[2] A remarkable aspect of the process is made clear when one compares the heights of the Au NWs and of the $SiO_2$

nanostructures obtained after the complete removal of the metal by IBS (AFM map in **Figure S1 d**). Indeed, the NWs of the Au mask are characterized by heights in the range 20-50 nm, while the vertical scale of the one-directional pattern in the $SiO_2$ extends up to 300 nm and the root-mean-squared roughness of the surface is of the order of 70-80 nm. The physical origin of the observed vertical amplification is related to the difference between the sputtering yields of the metal and of the substrate described above. It is worth noting that a proper choice of the mask and substrate materials (and of the sputtering yield ratio between them) allows for controlling the vertical scale amplitude of the surface features projected into the substrate.[1]

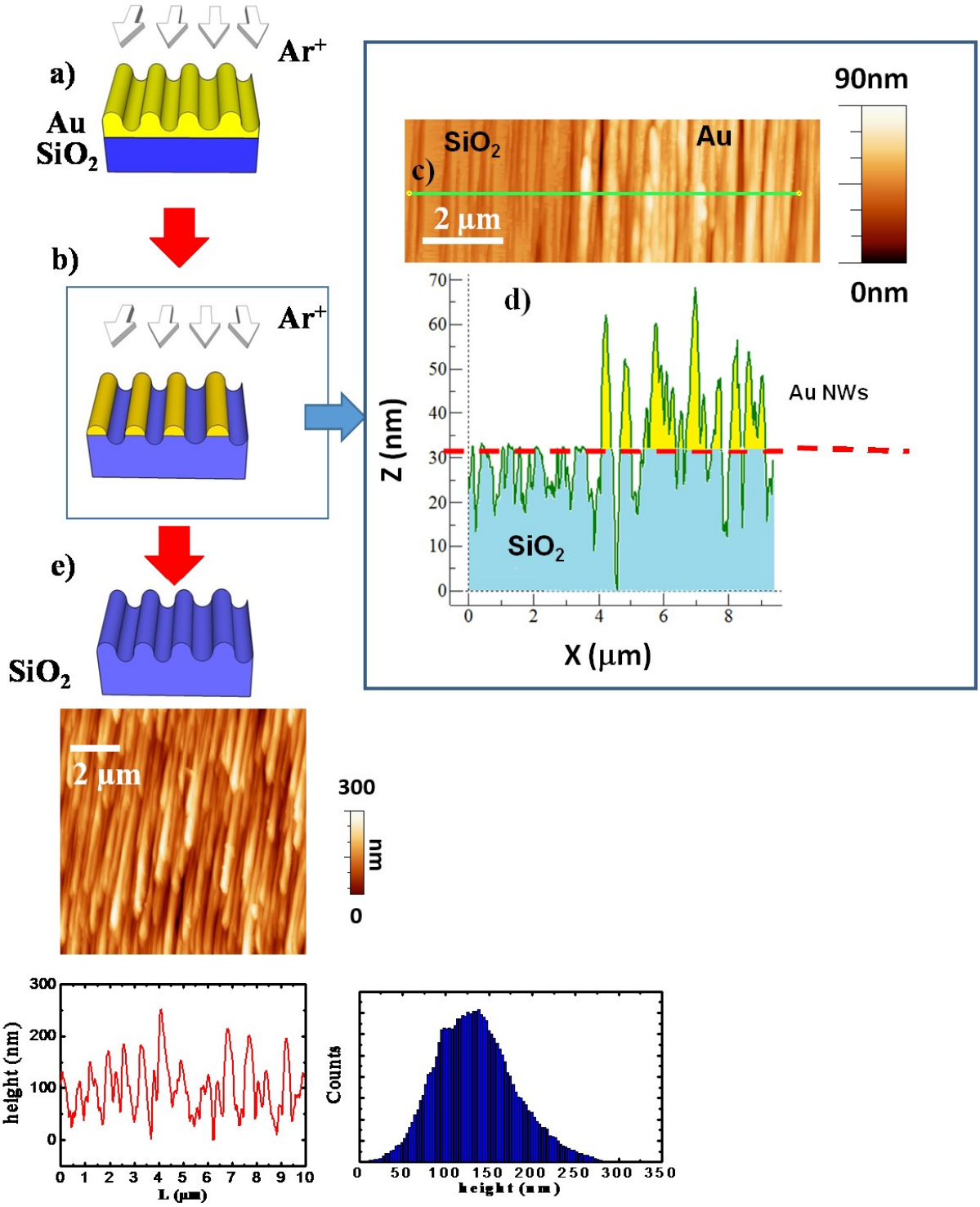


**Figure S1:** Process flow of the patterning process of the $SiO_2$ substrate: from the ripples formation on the surface of the sacrificial gold film (a), to the gold nanowires formation (NWs) (b), and to the transfer of the pattern into the substrate (e). (c) and (d) AFM investigation of the gold NWs array. (e) AFM topography of the $SiO_2$ substrate, a characteristic height profile and the histogram of the height distribution.

**Nanosheet formation** To further support the evidence of the $MoS_2$ nanosheets formation at the nanoscale, in **Figure S2** are shown the Energy Dispersive Spectroscopy (EDS) signal of the molybdenum and sulphur carried out by means of TEM. Comparison with the surface profile, shown on the right panel, reveals that molybdenum and sulphur signals follow conformally the spatial modulation of the substrate.

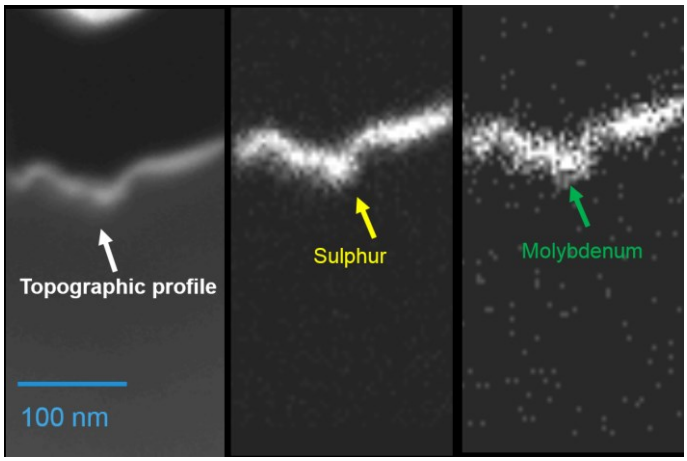


**Figure S2** Comparative study between a TEM micrograph of the surface profile (right) and EDS signals of Sulphur (at the center) and molybdenum (left) acquired by means of TM.

**Raman Spectroscopy:**

**Optical Dichroism** In order to assess to what extent the optical dichroism of the rippled sample affects the Raman spectra, we measured the total reflectance of the sample at different θ angles (angle between the incident polarization direction and the ripple orientation) by means of an integrating sphere setup. In **Figure S3 a** we report the trend of the reflectance as a function of θ=[0°,105°] at λ= 514 nm, the wavelength used in the Raman measurements. A clear modulation is observed in the reflectance plot: the minimum value, $R_{min}$, occurs at θ=0° while the maximum value, $R_{max}$, is found at θ=90°. It is worth noting that the dichroic ratio, defined as $[(R_{max}-R_{min})/(R_{max}+R_{min})]$, is of the order of ~ 0.03. Such an optical dichroism is then negligible when compared to the dichroic ratio calculated from the peak intensity of both the $E^1_{2g}$ and $A_{1g}$. Indeed, for the Raman modes, the dichroism is at least one order of magnitude larger than the one measured from the reflectance spectra, see **Table S1**.

| | $E^1_{2g}$ | $A_{1g}$ |
|---|---|---|
| $\frac{I_{max} - I_{min}}{I_{max} + I_{min}}$ | 0.48 | 0.64 |

**Table S1:** Dichroic ratio calculated from the peak intensity of the $E^1_{2g}$ and $A_{1g}$ Raman modes of the rippled nanosheets.

**$MoS_2$ peak intensity ratio** The isotropic behaviour of the Raman scattering for the reference flat $MoS_2$ nanosheets was inferred from the polar plot of the intensity ratio between the characteristic $A_{1g}$ and $E^1_{2g}$ peaks shown in **Figure S3 b** (black squares). It is worth noting that in single crystal $MoS_2$ nanosheets the intensity of the $A_{1g}$ mode varies as a function of the $\vartheta$ angle between the polarization vectors of the incoming and scattered photons, thus leading to an anisotropic polar distribution of the intensity ratio. [4] In our case, the flat $MoS_2$ sample consisted of polycrystalline $MoS_2$ grains randomly oriented in the sample plane. [5] This was a consequence of the CVD growth in which a thin molybdenum oxide film was employed as precursor for molybdenum. Moreover, in our polarized Raman measurements the polarization of the scattered photons was not detected and $\vartheta$ defines the angle between the incident laser polarization and the sample orientation. As a consequence, the CVD grown flat $MoS_2$ showed an isotropic polar dispersion of the Raman scattering signal. A further compelling evidence of the anisotropic Raman character of the rippled nanosheets respect to the flat ones is provided by the polar diagram of the $A_{1g}/E^1_{2g}$ intensity ratio plotted in **Figure S3 b** with red symbols. In this case the $A_{1g}/E^1_{2g}$ intensity ratio is intrinsically unaffected by the optical reflectivity of the patterned substrate. As such, the anisotropic angular distribution depicted in **Figure S3** corroborates the picture that the contribution of the dichroic reflectivity can be neglected in the study of the Raman spectra

**Raman peak broadening** Apart from the anisotropic behaviour and frequency shifts of the Raman modes reported in the main text, the deconvolution of the Raman peaks made evidence of a peak broadening in the rippled $MoS_2$ nanosheets with respect to the flat ones. From a careful study of the Raman spectra reported in **Figure S3 c**, it turned out that the deconvolution of the peaks required two

main Voigt components corresponding to the characteristic $E^1_{2g}$ and $A_{1g}$ modes (black curves in **Figure S3 c**). Nevertheless, an extra component (red curves) was necessary to take into account the broad shoulder aside the $E^1_{2g}$ peak at lower Raman shift (< 380 cm−1). The ratio between the areas subtended by the extra-component and the main one of the $E^1_{2g}$ mode is ~ 0.6 for the flat sample and ~1.23 for the rippled nanosheets. If on one hand, the value for the flat sample agrees with previous reports, on the other hand, the increased value for the rippled $MoS_2$ is compatible with the peak broadening triggered by the nanosheet bending already reported in wrinkled $MoS_2$ flakes.[6] Although we cannot rule out a contribution to the peak broadening arising from the presence of point defects as the origin of the extra-component in the flat nanosheets, we emphasize that point defects cannot explain the observed uniaxial modulation of the Raman and KPFM measurements in **Figure 3** and **4**. [7]

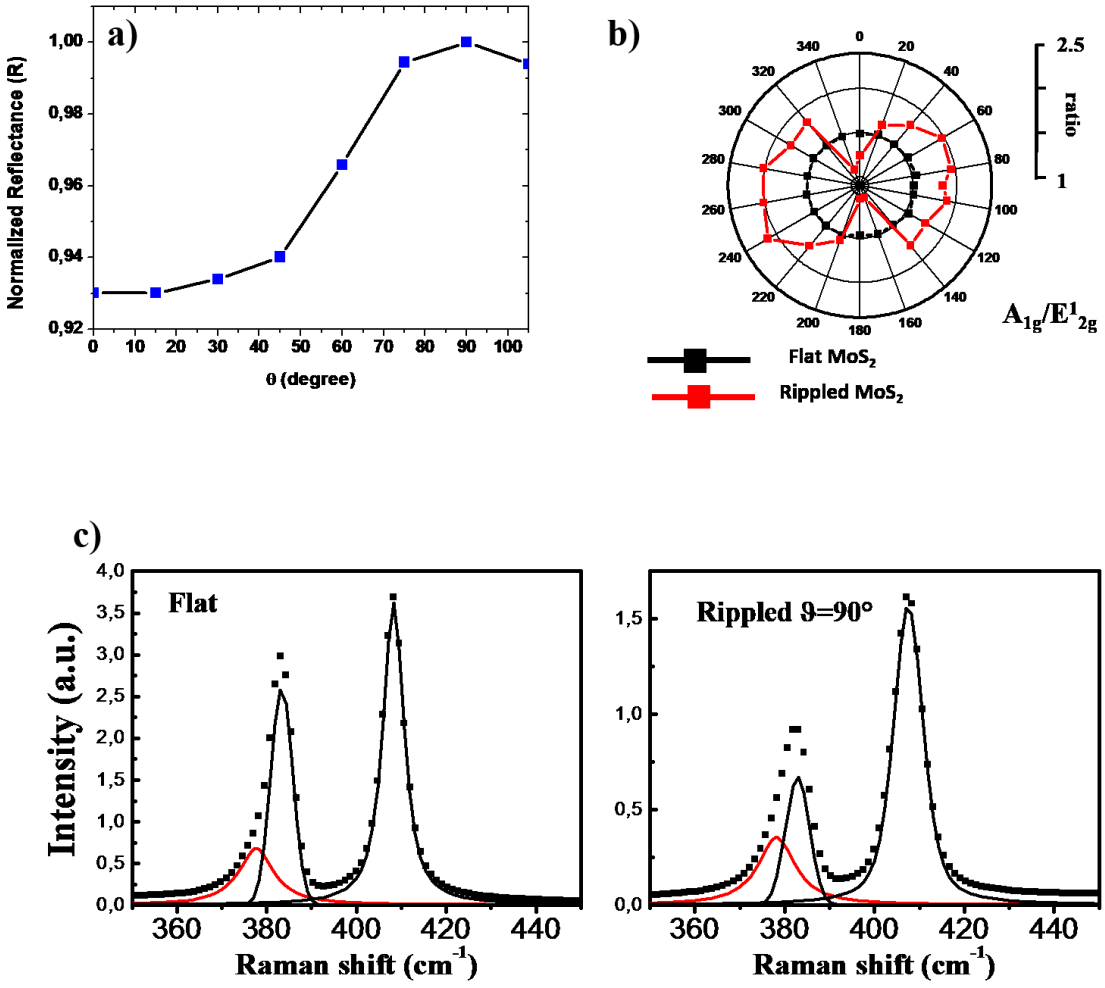

**Figure S3** a) Normalized Reflectance spectra of the rippled $MoS_2$ nanosheets as a function of the angle between the ripples axis and the incident polarization b) polar diagram of the intensity ratio $A_{1g}/E^1_{2g}$ for the flat sample (black squares) and rippled sample (red squares). c) Peak deconvolution for the flat (left) and rippled MoS2 nanosheets (right).

**Kelvin Probe Force Microscopy (KPFM).** To rule out technical artifacts in the KPFM measurements, the contact potential distribution (CPD) signal was first measured on the flat $MoS_2$ nanosheets across a scratch that was intentionally made in order to expose a region of the $SiO_2$ substrate (notice that the potential map was effective in reproducing the profile of the two materials, **Figure S4 a**). In **Figure S4 b** and **c** are shown the topographic and CPD maps acquired on a 6 μm x 6 μm sample area. The topographic map shows that the $MoS_2$ film completely covers the surface of the substrate and is characterized by a granular nature. In the inset of **Figure S4 c**, the white curve represents the histogram of the potential distribution in the $MoS_2$ area. It shows a symmetric line shape with a full-width-half-maximum (FWHM) of roughly ~500 mV. This large value is indicative of film inhomogeneity, that can be associated with the presence of surface contaminants or structural defects in the material (grains, vacancies, etc…).[5] In **Figure S4 d** the self-correlation functions for the CPD signal along the x- and y-axis (axis shown in the inset of **Figure S4 c**) are reported. Opposite to the rippled $MoS_2$ nanosheets, the decay of the self-correlation function occurs for both axis on a common length scale < 50 nm.

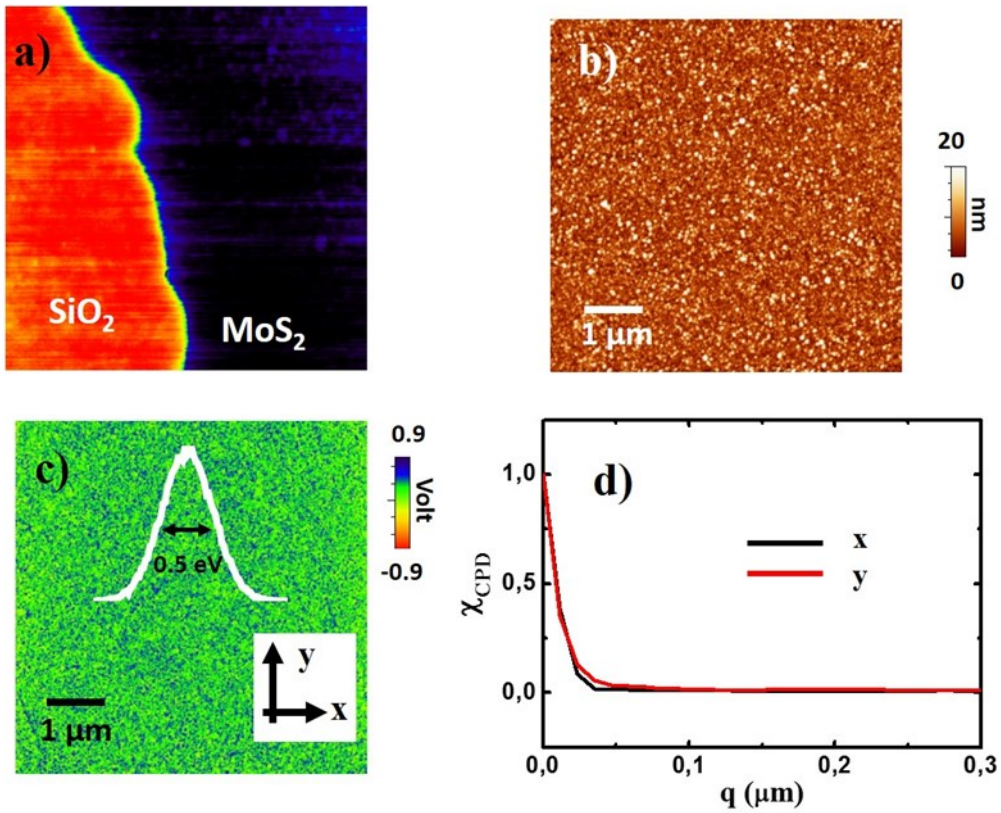


**Figure S4** (a) KPFM investigation across a mechanical scratch made in the flat $MoS_2$ nanosheets. (b) and (c) topographic and CPD maps acquired simultaneously on a 6 µm x 6 µm sample area, respectively. (d) Plot of the CPD self-correlation functions, $\chi_{CPD}$, calculated along the x and y directions shown in panel (c).

## Supporting Information References

[1] D. Chiappe, A. Toma, Z. Zhang, C. Boragno, F. Buatier de Mongeot, *Appl. Phy. Lett.* **2010**, 97, 53102.
[2] A. Toma, B. S. Batič, D. Chiappe, C. Boragno, U. Valbusa, M. Godec, M. Jenko, F. Buatier de Mongeot, *J. Appl. Phys.* **2008**, 104, 104313.
[3] C. Martella, D. Chiappe, C. Mennucci, F. B. de Mongeot, J. Appl. Phys. **2014**, 115, 194308.
[4] X. Zhang, X.-F. Qiao, W. Shi, J.-B. Wu, D.-S. Jiang, P.-H. Tan, *Chem. Soc. Rev.* **2015**, 44, 2757.
[5] S. Vangelista, E. Cinquanta, C. Martella, M. Alia, M. Longo, A. Lamperti, R. Mantovan, F. B. Basset, F. Pezzoli, A. Molle, *Nanotechnology* **2016**, 27, 10.

[6] A. Castellanos-Gomez, R. Roldán, E. Cappelluti, M. Buscema, F. Guinea, H. S. J. van der Zant, G. A. Steele, *Nano Lett*. **2013**, 13, 5361.
[7] S. Mignuzzi, A. J. Pollard, N. Bonini, B. Brennan, I. S. Gilmore, M. A. Pimenta, D. Richards, D. Roy, *Phys. Rev. B* **2015**, *91*, 195411